

## Mesoscale Impacts of Explicit Numerical Diffusion in a Convection-Permitting Model

WOLFGANG LANGHANS, JUERG SCHMIDLI, AND CHRISTOPH SCHÄR

*Institute for Atmospheric and Climate Science, ETH Zurich, Zurich, Switzerland*

(Manuscript received 4 October 2010, in final form 5 July 2011)

### ABSTRACT

In convection-permitting simulations, the spectrum of resolved motions is truncated near scales where convection is active. An “energy gap” between resolved and unresolved motions does not exist, such that the upscale and downscale fluxes of energy across the spectrum are affected by the representation of turbulence as well as (implicit and explicit) numerical diffusion. In the current study, a systematic analysis is undertaken of the role of explicit numerical diffusion in simulations of diurnal convection over a large Alpine region, using the Consortium for Small Scale Modeling (COSMO) mesoscale model. Results are explored by using energy spectra and by diagnosing the physical and dynamical contributions to the bulk mesoscale heat budget. In addition, a linear analytical model is employed to assess different formulations of numerical diffusion.

Consistent with previous studies the authors find that diffusion may strongly affect the energy spectrum and the formation of precipitation. Besides the direct impact on convective intensity and cloud distribution, they demonstrate that diffusion has an upscale influence and ultimately affects the mesoscale dynamics. Diffusion reduces the bulk Alpine net heating on a scale of  $O(100 \text{ km})$ . It is hypothesized that this upscale influence is primarily due to the following factor: multiple triggering of orographic convection over a complex mountain range leads to mountain-scale diurnal signals in vertical velocity that are sensitive even to scale-selective diffusion.

The simulations show that, in agreement with linear stability theory of convective growth, convective amplification is most sensitive to numerical diffusion of buoyancy and horizontal momentum components on near-surface model levels. If horizontal diffusion is not accomplished by a physically based parameterization and if the application of noise-reducing (e.g., monotonic) advection schemes proves to be insufficient to obviate the amplification of numerical noise, a necessary minimum of explicit diffusion is found to improve (i.e., decrease) the upscaling of energy to the mesoscale.

### 1. Introduction

During the last decade numerical weather and climate models have been pushing toward finer and finer grid spacings as a result of consistently growing computer capacities. Major benefits and advantages arise at kilometer-scale resolutions of  $O(1 \text{ km})$  compared to resolutions of  $O(10 \text{ km})$  or coarser.

Deep convective scales become partly resolved without the help of physical parameterizations of convective precipitation. Such convection-permitting models are capable of capturing the life cycle of moist convective features more realistically (Weisman et al. 1997; Lean and Clark 2003) and improve the timing of convective

initiation (e.g., Grell et al. 2000; Hohenegger et al. 2008; Lean et al. 2008). Also, small-scale topographic variations and spatial inhomogeneities in surface properties are better captured. Thus, the small-scale spatial distribution of precipitation over heterogeneous terrain is improved (Colle and Mass 2000; Zängl 2007).

Besides the aforementioned benefits, kilometer-scale simulations are known to under-resolve convective scales, since the energy containing characteristic turbulent length scales (and even smaller turbulent eddies) still partly remain at “subgrid” scales. A characteristic length scale of a few tens of meters was determined by Craig and Dörnbrack (2008) for a moist convective plume. Similarly, the studies conducted by Bryan et al. (2003) and Petch (2006) highlighted the need for grid spacings of  $O(100 \text{ m})$  in order to achieve convergence.

As a consequence, convection-permitting applications try to handle physically meaningful energy transport at poorly resolved scales, which are affected not only by

Corresponding author address: Wolfgang Langhans, Institute for Atmospheric and Climate Science, Universitätstrasse 16, 8092 Zurich, Switzerland.  
E-mail: wolfgang.langhans@env.ethz.ch

subgrid turbulent diffusion, but also by implicit and explicit numerical diffusion. Thus, the effective viscosity of the simulated fluid is not necessarily determined by the subgrid turbulent scheme alone, but also by the implicit dissipative properties of the applied numerical discretization scheme (Piotrowski et al. 2009) and eventually by explicit diffusion.

In principle, explicit (“artificial”) diffusion is not required in the case of upstream-biased diffusive numerical discretizations (Wicker and Skamarock 2002), but it still appears to be convenient and necessary to avoid the contamination of well-resolved scales by an amplification of grid-scale perturbations of numerical origin during specific situations. Such conditions typically occur during low wind speed, since the implicit damping of the upstream-biased schemes is proportional to the advective Courant number (e.g., Durran 1999, p. 85). Both idealized (Takemi and Rotunno 2003; Bryan 2005) and real-case studies (Knievel et al. 2007) reported poorly resolved convective features that grew within regions of neutral or unstable stratification and finally dominated the fields of horizontal divergence, vertical velocity, and cloud liquid water content. Applying increased explicit grid scale (and/or turbulent subgrid) diffusion may prevent the amplification of such errors.

In this paper impacts of explicit diffusion applied in convection-permitting simulations are investigated. Compared to some previous studies, we are not primarily interested in modifications of grid-scale-sized cloud structures, but in the mesoscale impact of the modified grid-scale behavior. Here, this sensitivity is explored by conducting simulations for a large Alpine region and for a period of strong localized thermally driven summertime convection. The mesoscale impact will be evaluated by both energy spectra and bulk heat budgets for the Alpine region.

Furthermore, the influence of explicit diffusion applied to specific prognostic variables will be addressed in this paper, since the amplification of a variable’s grid-scale perturbation does not necessarily depend equally on all prognostic variables. The latter aspect is also motivated by the fact that different numerical discretization schemes are commonly used for a subset of prognostic variables (e.g., Skamarock and Weisman 2009). An adequate convection-permitting simulation should not produce grid-scale fluctuations of numerical origin, which are subject to further amplification (Bryan 2005). On the other hand, the effective resolution of a simulation should not be deteriorated by unnecessarily strong explicit diffusion.

We simulate a period between 0000 UTC 11 July 2006 and 0600 UTC 20 July 2006, which has also been utilized for investigations of moist convection by Hohenegger

et al. (2008, 2009). During this period the synoptic constellation is formed by a high pressure system located over mid-Europe that provides fair-weather conditions, daytime radiative heating, and as a consequence, strong localized thunderstorms. The anomaly from the climatological mean temperature was around  $+5.0^{\circ}\text{C}$  and more than 15 hot days ( $\geq 30^{\circ}\text{C}$ ) had been observed in northern Switzerland during July 2006 (MeteoSchweiz 2006).

The outline is as follows. The mesoscale numerical model and the applied explicit numerical filter are described in section 2. Characteristics of a reference simulation without explicit diffusion are presented in section 3. The mesoscale impacts and its relation to grid-scale energy will be described in sections 4 and 5, respectively. In section 6 the linear theory of thermal instabilities is used to enhance our understanding of the impact of explicit diffusion on the growth of grid-scale perturbations. A discussion is presented in section 7 and the main results of this paper are summarized in section 8.

## 2. Methodology

### a. Model description and setup

The nonhydrostatic mesoscale NWP model of the Consortium for Small Scale Modeling (COSMO; Doms and Schättler 2002; Steppeler et al. 2003) is utilized at a resolution of  $\Delta x \approx 2.2 \text{ km}$ . Following Wicker and Skamarock (2002) the dynamics are based on a split-explicit third-order Runge–Kutta scheme (Förstner and Doms 2004) and a long time step of 30 s is used. A fifth-order upstream-biased discretization is applied for the horizontal advection. Vertical advection is computed implicitly using a centered second-order scheme. Moisture scalars and turbulence kinetic energy are advected both horizontally and vertically using the second-order positive-definite Bott scheme (Bott 1989). Other options for the advection of positive-definite scalars are available and their impact will be presented in section 5. The fully compressible governing equations are discretized on a staggered Arakawa-C grid with  $501 \times 451$  grid points that cover a large Alpine region of  $1100 \text{ km} \times 990 \text{ km}$  (see Fig. 1). Raymond’s (Raymond 1988) low-pass filter is applied to the underlying topography, such that little energy is contained at the grid scales. The 50% cutoff wavenumber  $k_c$  is given by

$$\epsilon^{-1} = \tan^{10}(k_c \Delta x / 2), \quad (1)$$

with  $\epsilon = 10$ , if not mentioned otherwise. The vertical coordinate is a height-based hybrid coordinate that gradually transforms from terrain-following levels at the bottom to plane levels at a 220-hPa level. The lowest of

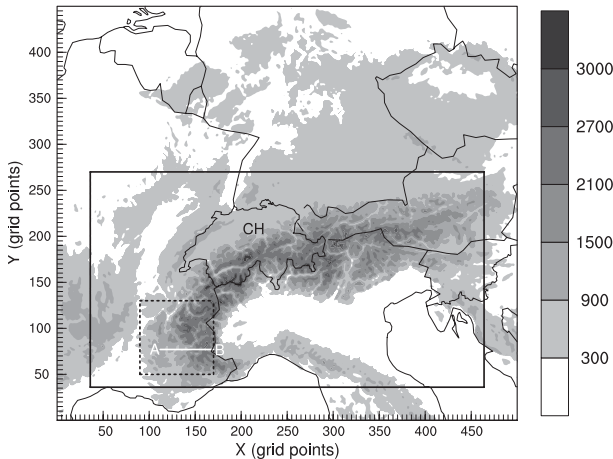


FIG. 1. Topography (m) of the model domain. The black box indicates the area used to compute spectra, the bulk heat budget tendencies, and mean precipitation rates. Note that the evaluation domain excludes the lateral frame with forcing from relaxation. The subdomain depicted by the dashed box is analyzed in Fig. 6 and the white line indicates the section shown in Fig. 3.

45 stretched mass levels is located  $\sim 33$  m above ground and the top 8 levels belong to a Rayleigh damping layer. The decision for this vertical coordinate was driven by its broad usage in the modeling community. Preliminary tests using a more recently developed vertical coordinate with smoother model levels (Schär et al. 2002) did not result in substantially different results for the convective summer period under investigation. Initial and lateral boundary conditions are provided every 6 h by the operational analysis of the European Centre for Medium-Range Weather Forecasts (ECMWF).

Subgrid-scale vertical turbulent diffusion is described by a diagnostic (turbulent kinetic energy) TKE-based scheme with a closure on level 2.5 (Raschendorfer 2001; Mellor and Yamada 1982). Thereby, the eddy-diffusion coefficients for heat  $K_H$  and momentum  $K_M$  are parameterized as

$$K_{H,M} = \lambda_l S_{H,M} \sqrt{2\text{TKE}}, \quad (2)$$

with the turbulent length scale  $\lambda_l$  formulated following Blackadar (1962) as

$$\lambda_l = \lambda_\infty \frac{\kappa z}{\kappa z + \lambda_\infty}. \quad (3)$$

An asymptotic turbulent length scale of  $\lambda_\infty = 100$  m is used.<sup>1</sup> Here  $S_{H,M}$  are stability functions for heat and

momentum, respectively, and  $\kappa$  is the von Kármán constant.

Other components within COSMO are the following: the radiative transfer scheme of Ritter and Geleyn (1992), a multilayer soil model (Heise et al. 2003), and a one-moment bulk cloud microphysics scheme with five prognostic hydrometeors (Reinhardt and Seifert 2006). Convective precipitation is assumed to be explicitly resolved.

### b. Explicit numerical diffusion

The explicit horizontal diffusion operator used within the COSMO model is a fourth-order monotonic filter, which is evaluated along model levels. Its implementation is for purely numerical purposes and the involved mixing does not intend to represent a physical diffusion process. The diffusive scalar flux is gradually decreased toward zero on steep model surfaces until a threshold of 250 m of height difference between two neighboring grid points is exceeded (Zängl 2002). Thereby, the upward mixing of moisture along terrain-following model surfaces can be avoided (Zängl 2004). The 2D diffusion operator appears as additional smoothing term in the budget equation of a prognostic variable  $\chi$ , in analytical form (here without limiters) written as

$$\frac{\partial \chi}{\partial t} = \dots - \nu_\chi \left( \frac{\partial^4 \chi}{\partial x^4} + \frac{\partial^4 \chi}{\partial y^4} \right).$$

Here,  $\chi$  is one of the following prognostic variables: pressure perturbation  $p'$ ; temperature perturbation  $T'$ ; the three velocity components  $u, v, w$ ; water vapor  $q_v$ ; and cloud liquid water  $q_C$ .

In general there is little objective guidance to define “ideal” values of the hyperviscosities  $\nu_\chi$ . For the following numerical experiments three diffusion coefficients  $\nu_1 = 3.0 \times 10^9 \text{ m}^4 \text{ s}^{-1}$ ,  $\nu_2 = 1.6 \times 10^9 \text{ m}^4 \text{ s}^{-1}$ , and  $\nu_3 = 1.0 \times 10^9 \text{ m}^4 \text{ s}^{-1}$  are used, which correspond to a damping by roughly 12%, 7%, and 4%, respectively, of the amplitude of the shortest resolved waves ( $\lambda = 2\Delta x$ ) per large time step. The corresponding nondimensional diffusion coefficients  $\alpha = \nu \Delta t / \Delta x^4$  are  $\alpha_1 = 3.8 \times 10^{-3}$ ,  $\alpha_2 = 2.1 \times 10^{-3}$ , and  $\alpha_3 = 1.3 \times 10^{-3}$ . The choice of these coefficients is in agreement with other models using fourth-order numerical diffusion. For instance Takemi and Rotunno (2003) perform WRF simulations using both weak diffusion with  $\alpha = 2.4 \times 10^{-3}$  and heavy diffusion with  $\alpha = 1.2 \times 10^{-2}$ .

Several sensitivity experiments will be conducted with diffusion applied to specific variables, and applied to specific model levels only. The specifications for all simulations are summarized in Table 1, with the naming convention chosen such that both the strength and the variables to be diffused can be identified. As an example

<sup>1</sup> This corresponds to a COSMO name list setting of  $\text{tur\_len} = \lambda_\infty/\kappa = 250$  m.

TABLE 1. Overview of all conducted numerical simulations. The applied diffusion coefficients are outlined for each variable ( $\nu_1 = 3.0 \times 10^9 \text{ m}^4 \text{ s}^{-1}$ ,  $\nu_2 = 1.6 \times 10^9 \text{ m}^4 \text{ s}^{-1}$ , and  $\nu_3 = 1.0 \times 10^9 \text{ m}^4 \text{ s}^{-1}$ ) and further description is given. For some simulations either a semi-Lagrangian (SL) or the van Leer (VL) moisture advection scheme is used, otherwise the positive-definite Bott second-order scheme.

Name	$\nu_{uv}$	$\nu_w$	$\nu_{T'}$	$\nu_q$
NODIFF	—	—	—	—
UVWPT1	$\nu_1$	$\nu_1$	$\nu_1$	$\nu_1$
UVW1	$\nu_1$	$\nu_1$	—	—
UVW2	$\nu_2$	$\nu_2$	—	—
UVW3	$\nu_3$	$\nu_3$	—	—
UV1	$\nu_1$	—	—	—
T1	—	—	$\nu_1$	—
Q1	—	—	—	$\nu_1$
W1	—	$\nu_1$	—	—
NODIFF_SL	—	—	—	—
NODIFF_VL	—	—	—	VL
Q1_SL	—	—	—	$\nu_1$
Q1_VL	—	—	—	VL
UVWPT1_A19	$\nu_1$	$\nu_1$	$\nu_1$	$\nu_1$
				Upper 19 (>3800 m AGL)
UVWPT1_L4	$\nu_1$	$\nu_1$	$\nu_1$	$\nu_1$
				Lowest 4 (<400 m AGL)
NODIFF_TOPO	—	—	—	Stronger filtered topography

simulation UVWPT1 uses the diffusion coefficient  $\nu_1$  on variables  $u$ ,  $v$ ,  $w$ ,  $p'$ , and  $T'$ .

### c. Budget diagnosis

The code of the model has been adapted such that all potential temperature and moisture scalar tendencies can be extracted. In this paper we utilize this tool to evaluate modifications of the components of the bulk heat budget within a large Alpine region.

Contributions to the budget equation for potential temperature, written as

$$\frac{\partial \theta}{\partial t} = \text{ADV}_\theta + Q_\theta^M + Q_\theta^T + Q_\theta^R + Q_\theta^{\text{HD}}, \quad (4)$$

are 3D advection  $\text{ADV}_\theta$ , latent heating  $Q_\theta^M$ , turbulent and radiative flux divergence  $Q_\theta^T$  and  $Q_\theta^R$ , respectively, and explicit horizontal diffusion  $Q_\theta^{\text{HD}}$ .

Computed tendencies from explicit numerical diffusion  $Q_\theta^{\text{HD}}$  will not be analyzed, as these tendencies revealed to be much smaller in magnitude than the others. Additionally, tendencies due to vertical advection are diagnosed each time step. All above-mentioned potential temperature tendencies are written hourly as time averages over all time steps between two output steps.

### d. Spectral analysis

Spectral analysis of atmospheric fields is used to further investigate the model's behavior at different scales (e.g., the grid scale and larger scales). Following Skamarock (2004) we mostly use averaged 1D real discrete Fourier transforms in both longitudinal and latitudinal direction to compute spectra at a certain altitude. Periodicity of the signals is achieved by removing the linear trend and split-cosine-bell tapering is applied to 10% of the signal to avoid leakage. This method is computationally less expensive than, for example the 2D discrete cosine transform (DCT) (Denis et al. 2002). Preliminary comparison of the two methods revealed the same response of spectral variance to numerical diffusion. Only averaged longitudinal spectra are shown below, as the response to explicit numerical diffusion is the same for both directions.

To analyze spatial energy distributions we also perform 2D Fourier transforms on periodic horizontal distributions of vertical velocity  $w$  of size  $2N - 1 \times 2M - 1$ , with  $N$  and  $M$  being the original number of grid points in each direction. To achieve periodicity the large field is constructed in the following manner: the bottom-left quadrant contains the original  $w$  distribution, while quadrants two to three contain its mirror image in  $x$ , both  $x$  and  $y$ , and  $y$  direction, respectively.

To distinguish between small-scale and large-scale spectral contributions, we extract low-frequency modes by removing all coefficients of modes with wavenumbers larger than  $n = 20$  ( $\lambda_x = 110 \text{ km}$ ) or  $m = 18$  ( $\lambda_y = 110 \text{ km}$ ). The transformation using the sharp spectral filter is then given by

$$\hat{w}(n, m) = \begin{cases} \frac{1}{(2N - 1)(2M - 1)} \sum_{k=0}^{2N-2} \sum_{l=0}^{2M-2} w(k, l) e^{-i[2\pi nk/(2N-1) + 2\pi ml/(2M-1)]} & \{n \leq 20\} \cap \{m \leq 18\} \\ 0 & \{n > 20\} \cup \{m > 18\}. \end{cases}$$

The backward transformation yields the large-scale part of  $w$  with wavelengths  $\lambda \geq \lambda_{\text{cut}} = (\lambda_x^2 + \lambda_y^2)^{1/2} = 155.73 \text{ km}$ . The cutoff wavenumbers have been chosen to be small

enough to sufficiently reduce small-scale energy and large enough to account for a sufficiently large number of low-wavenumber modes.

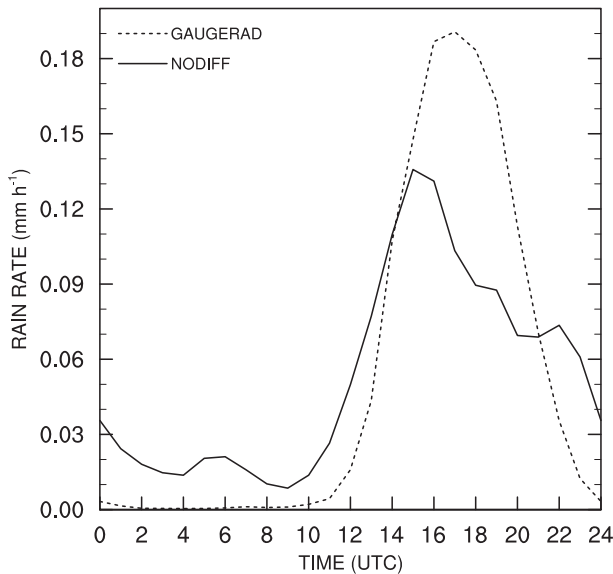


FIG. 2. Simulated mean diurnal cycle of precipitation ( $\text{mm h}^{-1}$ ) from NODIFF averaged over Switzerland (indicated by “CH” in Fig. 1) and between 0600 UTC 11 Jul 2006 and 0600 UTC 20 Jul 2006. Observational data GAUGERAD [for explanation see Wüest et al. (2010)] are added for comparison and simulated precipitation rates are only used at grid points where interpolated observational measurements are available.

### 3. Reference run without explicit diffusion

#### a. Precipitation

Before the impacts of numerical diffusion are described in this section we analyze the performance of the simulation without explicit numerical diffusion (NODIFF). Figure 2 shows the mean diurnal cycle of simulated precipitation averaged spatially over Switzerland and computed for the 9-day period. Also shown are daily surface-based rain measurements that have been disaggregated using radar measurements [GAUGERAD; see Wüest et al. (2010) for explanation]. The timing of the precipitation peak in Switzerland produced by NODIFF is in agreement with the observations. Also the total precipitation in Switzerland is captured quite well (see also Table 2), although the diurnal cycle reveals underestimations during daytime and overestimations during nighttime.

#### b. Heat tendencies of single convective plumes

To understand the potential temperature forcings that are involved in the process of moist convection, the heat tendencies of single convective plumes are studied before we describe the bulk Alpine heating below. Typically, convective cells are released from a dry static unstable near-surface layer. As an example, Fig. 3 shows a vertical cross section of an unstable near-surface layer

TABLE 2. Relative deviation (%) of simulated accumulated ( $\text{TOT}_{\text{CH}}$ ) and mean peak precipitation ( $\text{PEAK}_{\text{CH}}$ ) from observed precipitation in Switzerland and relative reduction of accumulated ( $\text{TOT}_{\text{ALPS}}$ ) and mean peak precipitation ( $\text{PEAK}_{\text{ALPS}}$ ) due to explicit numerical diffusion in the Alpine subregion. Modifications of  $\text{TOT}_{\text{ALPS}}$  and  $\text{PEAK}_{\text{ALPS}}$  are calculated with respect to NODIFF, but with respect to Q1 for simulations Q1\_SL and Q1\_VL.

Run	$\text{TOT}_{\text{CH}}$	$\text{PEAK}_{\text{CH}}$	$\text{TOT}_{\text{ALPS}}$	$\text{PEAK}_{\text{ALPS}}$
NODIFF	-0.6	-28.8		
UVWPT1	-38.0	-55.8	-37.3	-32.3
UVW1	-31.9	-51.4	-27.8	-25.6
UVW2	-17.9	-46.1	-20.2	-15.9
UVW3	-12.2	-35.3	-16.1	-14.2
UV1	-30.2	-51.1	-27.3	-24.1
T1	-27.5	-43.6	-29.1	-27.6
Q1	-4.0	-34.2	-6.1	-4.2
W1	-5.0	-32.2	-6.5	-8.4
NODIFF_SL	28.3	22.7	10.3	34.4
NODIFF_VL	8.7	-17.8	3.8	4.6
Q1_SL	-10.3	-19.9	3.3	11.0
Q1_VL	-14.5	-32.7	1.3	3.1
UVWPT1_A19	5.2	-23.8	-0.8	1.1
UVWPT1_L4	-38.0	-59.5	-34.9	-39.0
NODIFF_TOPO	-25.5	-47.9	-24.1	-27.2

at 1300 UTC 17 July 2006 (Fig. 3a) and the contributions to the atmospheric heat budget (Figs. 3a–d). Advection cools potential temperatures within moist convective updrafts (Figs. 3a,b), since air parcels are rising in dry stably stratified air (see also Fig. 3a). The immediate environment of (as well to a lesser degree the space in between) convective cells is heated by advection, as compensating subsidence transports potentially warmer air toward lower levels (Fig. 3b).

Within saturated regions the large advective cooling is outbalanced by the release of latent heat (Fig. 3c), while evaporation cools the subsaturated surroundings of single cells. The lowest model levels are heated because of turbulent flux convergence (Fig. 3d). Furthermore, subgrid mixing in each single convective plume involves a pattern of heating and cooling as it penetrates through the top of the PBL.

#### c. Diurnal cycle of the bulk heat tendencies

Figure 4 shows the mean diurnal cycle of the bulk Alpine net heating and each of the contributing potential temperature tendencies for simulation NODIFF. The tendencies have been spatially averaged over the large Alpine subdomain shown in Fig. 1. In the lowest 2 km net cooling dominates between the early afternoon and the early morning, while during daytime the heating gradually extends from close to the surface at 0700 UTC to higher elevations at roughly 4 km and also affects the upper troposphere between 1300 and 1800 UTC (see Fig. 4a). The maximum heating at low levels is reached

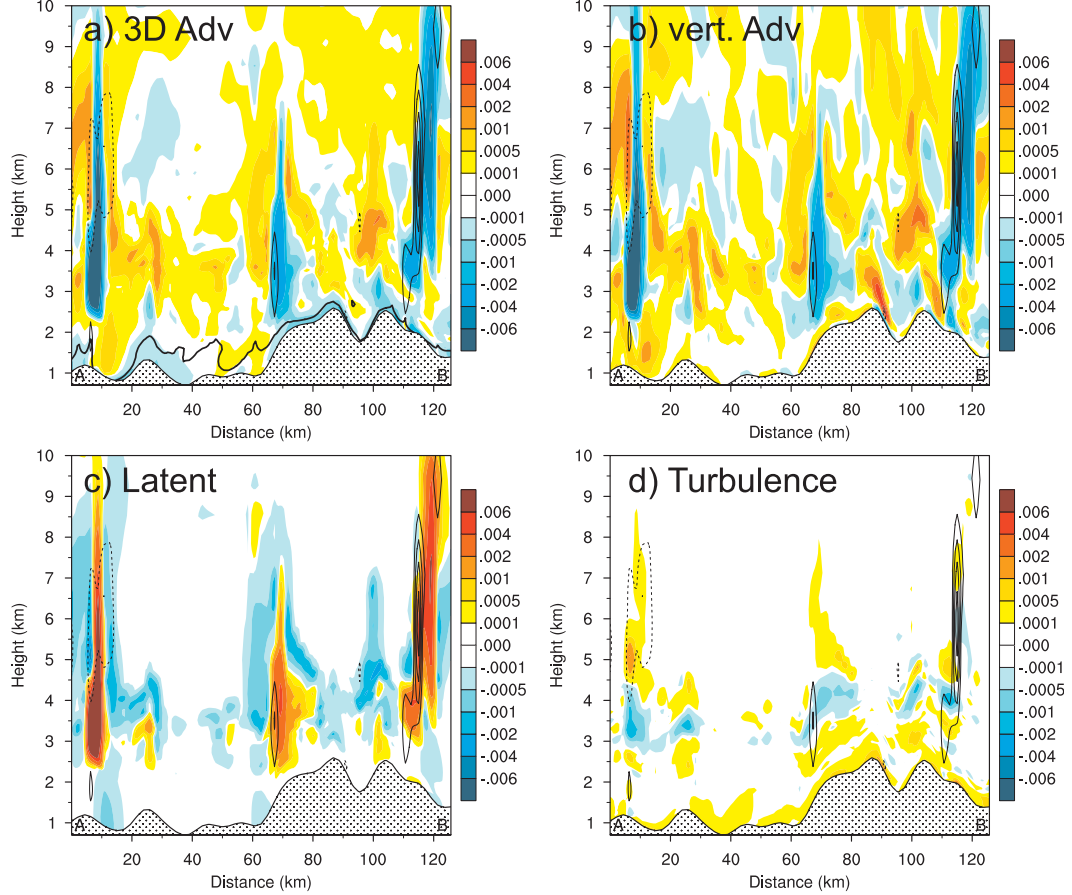


FIG. 3. The potential temperature tendencies ( $\text{K s}^{-1}$ , colors) from NODIFF due to (a) advection, (b) vertical advection, (c) microphysics, and (d) turbulence are shown as average over all time steps between 1200 and 1300 UTC 17 Jul 2006. Vertical velocity [ $1 \text{ m s}^{-1}$  interval, solid (dashed) black contours for positive (negative values)] in (a)–(d) has been averaged between two instantaneous output values (1200 and 1300 UTC). The region below the thick black contour in (a) corresponds to negative values of  $N^2$ . The position of the vertical slice is indicated in Fig. 1.

at 1100 UTC and the upper troposphere is heated strongest around 1500 UTC. Obviously, the strong low-level daytime heating results mainly from turbulent flux convergence within the PBL (see Fig. 4e) and also partly from radiative heating (see Fig. 4f).

With the onset of condensation, the warming is increased by the release of latent heat above  $\sim 3$  km MSL (see Fig. 4d) and is strongest around 1600 UTC at  $\sim 8$  km MSL. Below  $\sim 3$  km evaporative cooling dominates the mean microphysics tendencies until the first half of the night.

Potential temperature advection (see Fig. 4b) is responsible for the net warming between  $\sim 1.5$  and  $\sim 10$  km, which is interrupted only by a period of cooling between 1400 and 1900 UTC. The advective warming is a consequence mainly of the large-scale subsidence (see Fig. 4c), which is overcome only by upward transport of potentially cooler air due to moist convection (see Figs. 4c and 3a,b). Apparently, the midday heating by vertical transpor-

within the PBL (see Figs. 4c and 3b) is partly compensated for by horizontal advection, since at this time the total advection (Fig. 4b) provides a cooling also at the  $\sim 2$ -km level, but particularly farther below. A thermally driven plain–mountain circulation is found to be the driving mechanism for this continuous low-level cooling. As described by (e.g., Schmidli and Rotunno 2010), the thermal wind between plains and mountainous regions blows along the potential temperature gradient and therefore advects cooler temperatures.

#### 4. The impact of explicit diffusion

##### a. Precipitation

In this section a description of the impacts of numerical diffusion is given. We begin our analysis with precipitation rates and address the small-scale influence before the mesoscale impact will be described. Figure 5

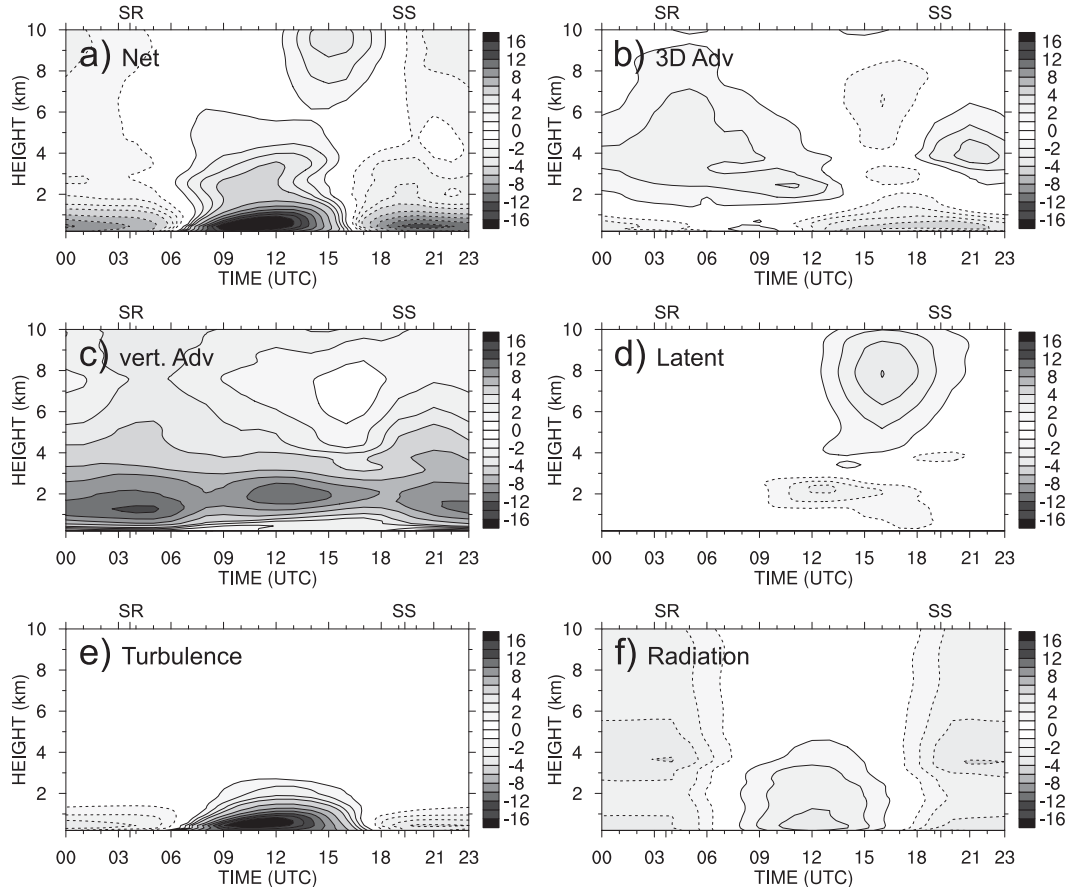


FIG. 4. Mean diurnal cycle of potential temperature tendencies ( $10^{-5} \text{ K s}^{-1} = 0.86 \text{ K day}^{-1}$ ) from simulation NODIFF: (a) net heating, (b) total advection, (c) vertical advection, (d) latent heating, (e) turbulent flux divergence, and (f) radiative flux divergence. The tendencies have been averaged spatially over the Alpine subdomain indicated in Fig. 1 and from 0600 UTC 17 Jul 2006 to 0600 UTC 20 Jul 2006. The height axis starts at 200 m, since lower altitudes would correspond to grid points over the Po valley only. Sunrise and sunset are indicated by "SR" and "SS", respectively.

shows the mean diurnal cycle of precipitation averaged spatially over a large Alpine region (solid box in Fig. 1). Obviously, the deficits of the reference run NODIFF are also characteristic for simulations applying diffusion. The (under) overestimation during (day) nighttime indicate that this specific issue is governed by other factors than explicit numerical diffusion.

The highest precipitation rates are produced by NODIFF during the afternoon. Adding explicit diffusion significantly decreases the mean peak precipitation in all other simulations (see Fig. 5). The strongest reduction of the peak precipitation rate by 32% is found for simulation UVWPT1 (see also Table 2); the accumulated precipitation is even reduced by 37%. Reductions in mean peak precipitation by 28% and 24% are produced by simulations T1 and UV1, respectively. Primarily, numerical diffusion seems to reduce grid-scale perturbations responsible for convective growth.

Interestingly, simulations W1 and Q1 reveal an almost negligible influence of explicit diffusion. This is in line with the fact that UVW1 does not further decrease precipitation compared to UV1. A similar response of convective precipitation to explicit diffusion is found for averaged rain rates in Switzerland (see also Table 2).

#### b. Spectral analysis

Moist convective clouds are produced by all simulations, although intensity, size, and number of cells vary among the simulations. Distributions of vertical velocity and cloud water at 4 km MSL at 1200 and 1600 UTC 17 July 2006 are shown in Figs. 6a–h for a small subdomain located over the southwestern part of the Alpine barrier (see Fig. 1). Note that in Fig. 6 only a selection of all simulations is shown, since the cloud distributions are similar for some runs. In general, cloud sizes appear to be smaller around midday (Figs. 6a–d) than during the

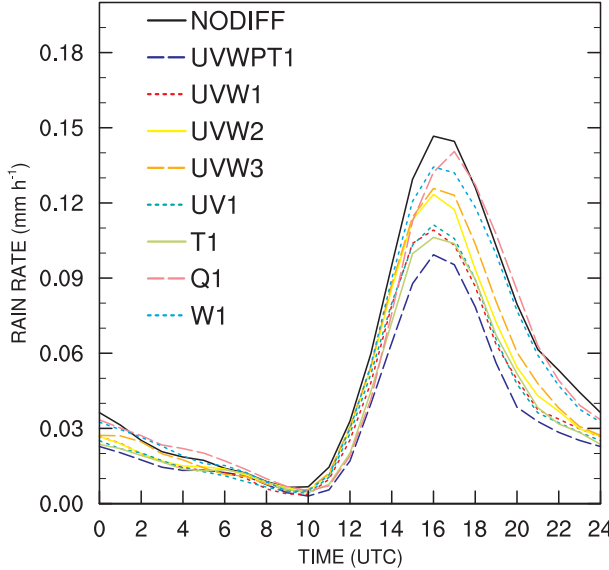


FIG. 5. As in Fig. 2, but for simulations applying numerical diffusion. Precipitation has been averaged over an Alpine subdomain (solid black box in Fig. 1).

afternoon (Figs. 6e–h). Particularly NODIFF reveals numerous grid-scale cloud features at 1200 UTC. This tendency to produce numerous small and strong updrafts is still apparent at 1600 UTC (Fig. 6e). The intensity exceeds  $8 \text{ m s}^{-1}$  in many plumes. These small-scale features reveal some similarity with Takemi and Rotunno's

(2003) so-called grid-scale “diamonds,” which were visible in simulations with too weak small-scale diffusion. Too numerous and too small convective cells have also been reported by Lean et al. (2008).

Compared to NODIFF the number of distinct grid-scale clouds is drastically decreased in simulations UVWPT1 (Figs. 6b,f), UVW1 (Figs. 6c,g), and UV1 causing smoother distributions. The largest vertical velocity in UVWPT1 is around  $5 \text{ m s}^{-1}$  at 1600 UTC and cells appear to be of larger size. The tendency to produce larger cloud structures can also be identified from UVW2 and UVW3, although the latter tends to produce some grid-scale clouds (not shown). Astonishingly, W1 (Figs. 6d,h) seems to have little impact on the size and number of convective plumes as moist convection is frequently initiated at very small scales, particularly around midday. The impact of diffusion seems to depend on the applied magnitude of the diffusion coefficient *and* on the prognostic variable to be diffused. One might suppose that the insensitivity (sensitivity) to explicit diffusion of vertical (horizontal) velocity is linked to the fact that convection is primarily triggered by horizontal convergence. Still, diffusion of vertical velocity could directly suppress the convective growth. A theoretical explanation for this asymmetric response will be given in section 6.

To bridge the gap between cloud scales and the mesoscale and to cope with the complexity induced by the stochastic component of convection, spectral analysis is

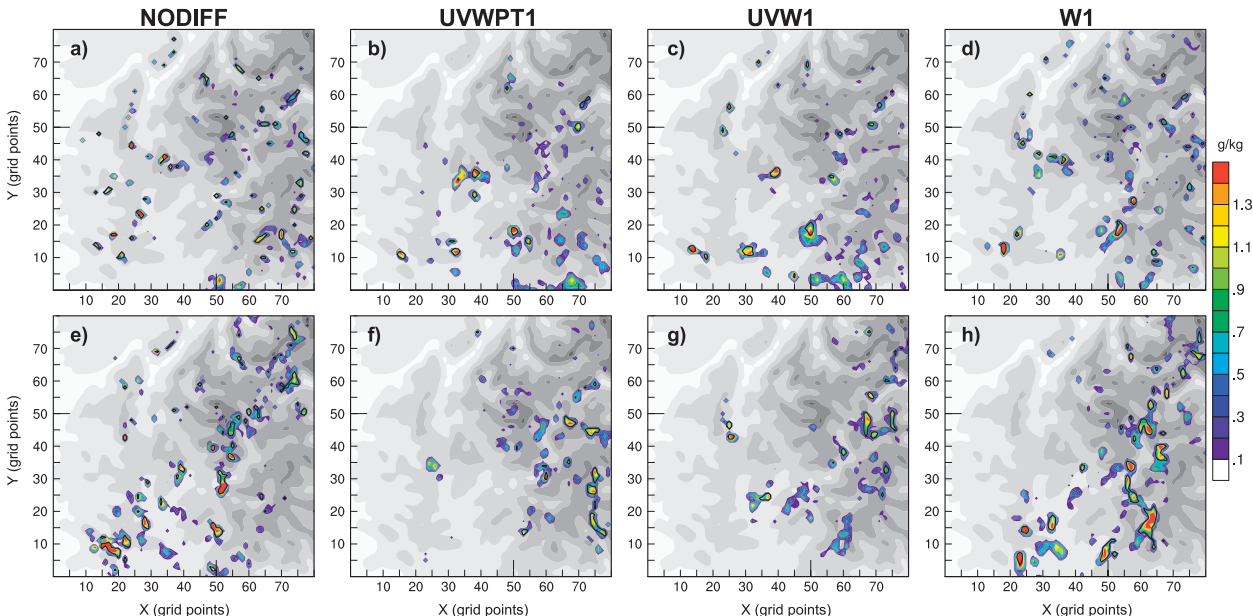


FIG. 6. Horizontal fields of cloud water ( $\text{g kg}^{-1}$ , colored) at 4 km MSL at (a)–(d) 1200 UTC and (e)–(h) 1600 UTC 17 Jul 2006 obtained from simulation (a),(e) NODIFF; (b),(f) UVWPT1; (c),(g) UVW1; and (d),(h) W1. Also shown is the  $2 \text{ m s}^{-1}$  vertical velocity contour (black). The topography is shaded (grayscale) every 600 m. The position of the subdomain shown is indicated in Fig. 1.

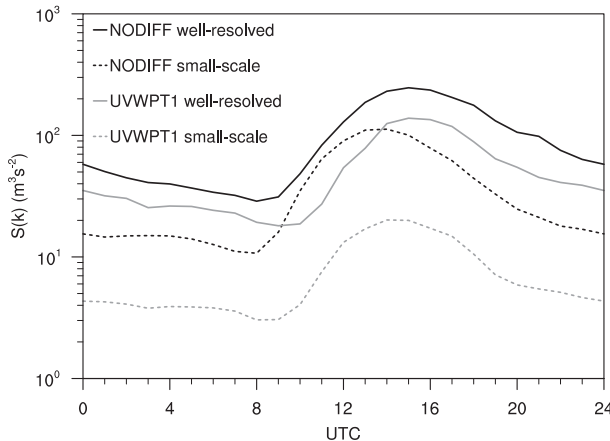


FIG. 7. Mean diurnal cycles of spectral energy density computed for vertical velocity at 4 km MSL from simulations NODIFF and UVWPT1. Densities have been averaged over well-resolved scales with  $517 \text{ km} > \lambda > 20 \text{ km}$  and small scales with  $10 \text{ km} > \lambda > 2\Delta x$ .

used in the following to analyze the impacts of explicit diffusion. At first, the mean diurnal cycle of well resolved and small-scale spectral variance of vertical velocity at 4 km MSL is discussed for NODIFF and UVWPT1. Figure 7 indicates a continuous energy input at the small scales between 0800 and 1300 UTC in NODIFF; afterward the energy decays steadily. The large-scale energy peak is reached with a delay of 2 h at 1500 UTC in NODIFF (Fig. 7), such that comparable amounts of energy are contained in well-resolved and small-scale motions around 1100 UTC.

In UVWPT1 the period of grid-scale energy input starts 1 h later than in NODIFF and lasts even until 1500 UTC. Then the energy at small scales is only as large as the energy at 0900 UTC in simulation NODIFF. Even the energy contained in well-resolved scales is reduced throughout the day.

For all simulations, spectra of vertical velocity at 4 km MSL and at 1600 UTC are shown in Fig. 8. Similar to the findings presented in Gage and Nastrom (1985) spectral densities of vertical velocity reveal a generally “flat” energy distribution in the mesoscale. The  $2\Delta x$  waves are filtered most effectively by a factor of 8 in simulation UVWPT1. In all other simulations the grid-scale variance is reduced less. At  $\sim 7\Delta x$  most of the variance is produced by simulation NODIFF, while the strongest diffusion results from UVWPT1, UVW1, UV1, and T1; reductions of energy by W1 are as small as in simulations using weak and intermediate diffusion of momentum (UVW2, UVW3).

Besides impacts on the model cloud scales, also the well-resolved Alpine scales are substantially modified. The T1 produces the most effective decrease in variance

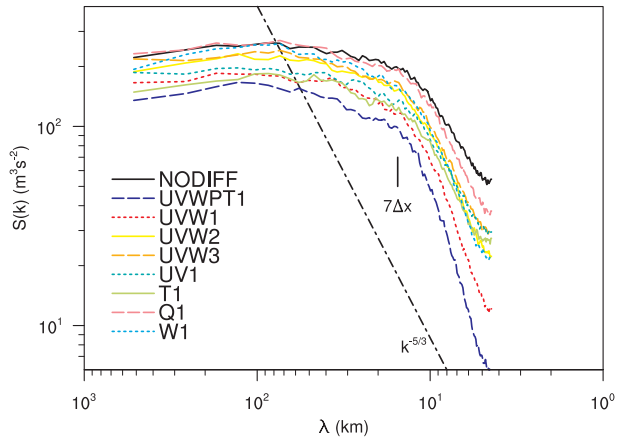


FIG. 8. Mean spectra of vertical velocity computed for the Alpine subdomain at 4000 m MSL. The spectral densities obtained from the simulations have been averaged for 1600 UTC when convective updrafts are strongest. The  $5/3$  power law is indicated by the dashed-dotted line.

at the well-resolved scales, which is only outreach by simulation UVWPT1 (see Fig. 8). The reduction of large-scale variance increases with the strength of the damping of momentum (UVW1, UVW2, and UVW3). The smallest decrease at Alpine scale and mesoscale corresponds to simulations Q1 and W1 (see Fig. 8). This large-scale impact is also found for total kinetic energy. Note that simulations Q1 and W1, which exhibit high variance at the mesoscale also produce large precipitation peaks and sums, whereas the decline of mesoscale energy in the other simulations is in agreement with the reduction of convective precipitation (see Fig. 5 and Table 2).

To clarify the intensity of the energy reductions the ratio of spectral energy density between UVWPT1 and NODIFF is shown in Fig. 9. The explicit diffusion removes the grid-scale energy quite consistently by 80%–90% at 4 km MSL (Fig. 9) and affects also significantly larger scales, although multiple applications of the filter response (black analytical curve) would support a more scale-selective filter response. The impact on energy at larger scales is strongly dependent on the time of day with significantly smaller reductions during the morning than around midday or the late evening. Only  $\sim 40\%$  of the energy remains at large scales at 1000 and 1200 UTC, which is much less than expected from explicit diffusion alone.

There are several hypothesis to explain this behavior. First, the encountered influence on dynamics at different scales might be excited by propagating gravity waves that are triggered by convective plumes. This hypothesis is based on the findings by VanZandt (1982), who explained the spectral kinetic energy distribution in the

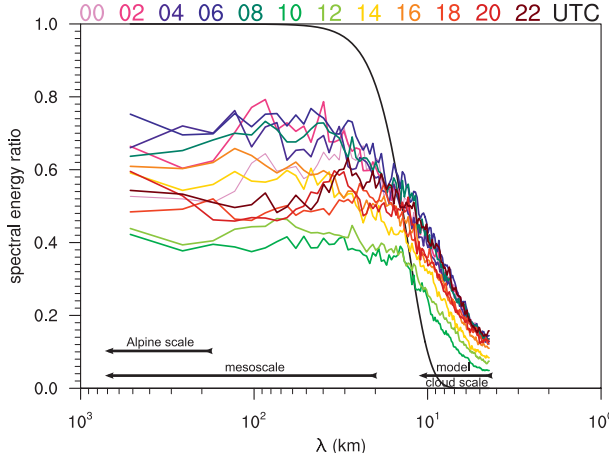


FIG. 9. The diurnal cycle of the ratio of spectral energy densities between simulations UVWPT1 and NODIFF. Mean spectra are computed for vertical velocity at 4 km MSL and time is given in UTC. The discretized response function of the fourth-order filter given by  $(1 - 2\alpha_1[2[1 - \cos(k\Delta x)]])^2)^n$  using a hyperviscosity  $\alpha_1 = 3.8 \times 10^{-3}$  is indicated by the black solid line for  $n = 120$  large time steps ( $=1$  h).

mesoscale with the help of a buoyancy wave model. Second, the large-scale influence could also be a consequence of a stronger Alpine-scale “pumping” of air mass, a dynamical process studied by Weissmann et al. (2005). Third, triggering of multiple orographic convective cells scattered over the Alpine rim might directly form an Alpine-scale signal in vertical velocity. Likely, hypotheses two and three are closely linked and difficult to isolate.

To identify the process responsible for Alpine-scale vertical motion, we use 2D Fourier transformation and decompose the wave spectrum into a large- and small-scale contribution (see section 2). The average horizontal distribution of the large-scale vertical velocity at 8 km MSL and 1600 UTC is shown for NODIFF and UVWPT1 in Fig. 10. In simulation NODIFF strong

large-scale lifting occurs over the southwestern Alpine crest and at some locations over the eastern parts of the Alps (Fig. 10a). These signals, together with the compensating downdrafts, are significantly reduced in UVWPT1 (see Fig. 10b). Analysis of the accumulated precipitation pattern (see Figs. 10a,b) and the small-scale vertical velocity field (not shown) reveals a spatial agreement with the regions of strong large-scale vertical velocity. Thus, in contradiction to the first hypothesis, the mesoscale impact on the spectral densities is a direct consequence of small-scale convective activity. The result is consistent with the idea of many small-scale plumes merging into a mesoscale ascending region. Since also the intensity of the “alpine pumping” is significantly reduced by the small-scale diffusion (see Fig. 10b), it is difficult to disentangle hypotheses two and three.

### c. Impacts on the bulk Alpine heat budget

Simulation UVWPT1 results in substantially altered bulk heat tendencies, as can be seen in Fig. 11, which shows the absolute differences to the bulk tendencies of NODIFF. For better comprehension we also calculated the relative modifications of selected peak tendencies (i.e., the relative modification of maxima and minima with respect to NODIFF). The net heating during daytime is decreased in UVWPT1 within the PBL between 0900 and 1500 UTC and also later in the upper troposphere (Fig. 11a), where the heating peak is reduced by 30%. A net gain in heating is produced during 1600 and 2100 UTC within the lowest 5 km. The modifications of the budget components show that especially the dynamics (i.e., the potential temperature advection; Figs. 11b,c) and the latent heating (Fig. 11d) are both modified substantially. The advective cooling peak at upper levels (shown in Fig. 4b) is decreased by 69%, which is counteracted by a reduction in latent heating by 51%. Figure 11c underlines the modified dynamical behavior with less heating by vertical advection within the PBL

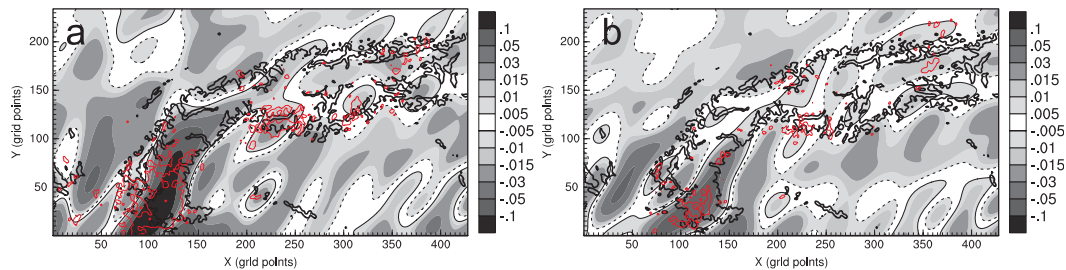


FIG. 10. Mean large-scale vertical velocity patterns ( $m s^{-1}$ ) at 8 km MSL and 1600 UTC from simulation (a) NODIFF and (b) UVWPT1. A cutoff wavelength of  $\lambda_{cut} \approx 150$  km has been applied to decompose the fields (see also section 2). The thin solid (dashed) contour line isolates positive (negative) values. The red line shows the 50-mm contour of a slightly smoothed distribution of total accumulated precipitation. Topography within the subdomain is indicated by the thick black line at 1200 m MSL.

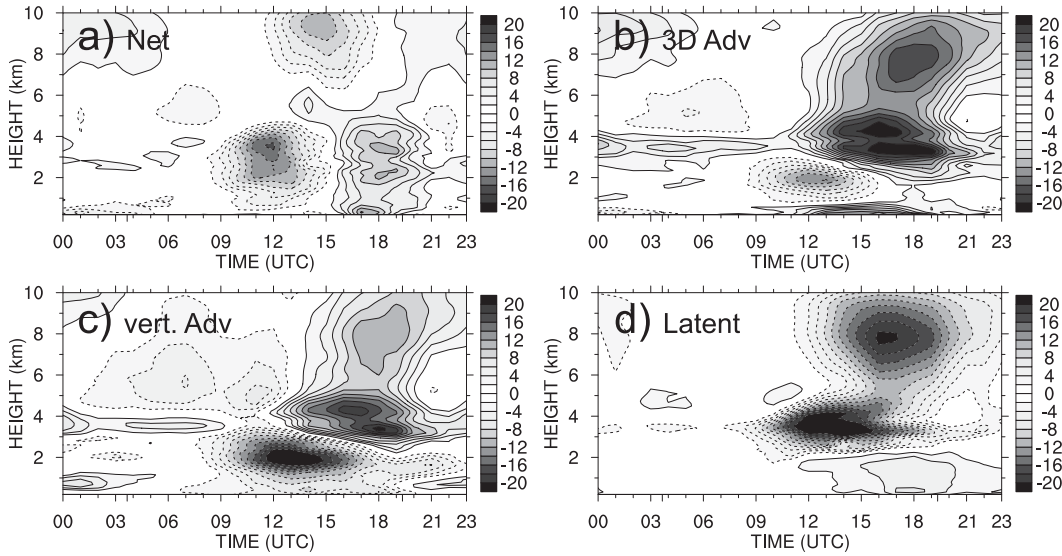


FIG. 11. As in Fig. 4, but for the difference between potential temperature tendencies in UVWPT1 and NODIFF ( $10^{-6} \text{ K s}^{-1}$ ): (a) net heating, (b) total advection, (c) vertical advection, and (d) latent heating. The contour increment is  $2 \times 10^{-6} \text{ K s}^{-1}$  and solid (dashed) lines indicate positive (negative) values [i.e., an increase (decrease) in heating] compared to NODIFF.

and increased heating above  $\sim 3$  km MSL. The applied numerical diffusion does not significantly affect the tendencies from subgrid turbulence and radiation parameterizations (not shown).

The bulk heat budget in the other sensitivity experiments is affected less, but still significant modifications also result from diffusion of only specific prognostic variables. As an example, diffusion in T1 decreases the net heating in the upper troposphere by 22%. Interestingly, applying diffusion in W1 results in a reduction

of the tropospheric net heating by only 8% (see also Fig. 12a) and advective tendencies are marginally modified (Fig. 12b). The impact reveals to be smaller than in simulation UVW3, for which weaker diffusion is applied, but on all three momentum components. This is in agreement with the large precipitation rates and high spectral densities of W1 at well-resolved scales.

Compared to NODIFF the bulk net heating in the upper troposphere is minimized by 19%, 12%, and 9% in simulations UV1, UVW2, and UVW3, respectively.

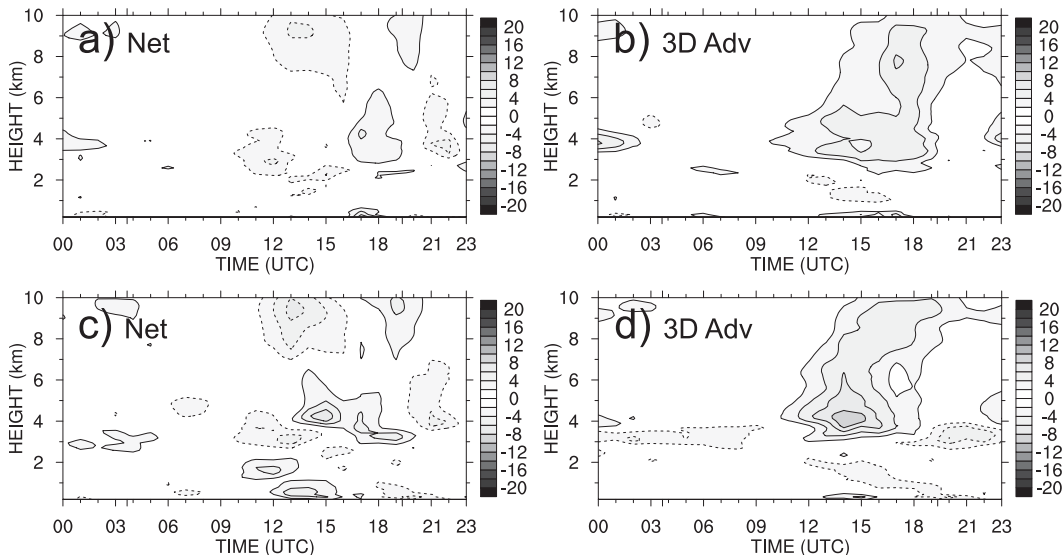


FIG. 12. As in Fig. 11, but for simulation (a),(b) W1 and (c),(d) Q1: (a),(c) net heating and (b),(d) total advection.

Equivalently, the budget components in UVW1, UVW2, and UVW3 are modified less drastically with decreasing filter magnitude, but still the reduction of latent heating and advective cooling amounts to 20% and 25%, respectively, for simulation UVW3.

Finally, Q1 results in only small modifications of the net tendencies (Fig. 12c) and the advective tendencies (Fig. 12d), which is in line with the large precipitation rates and unmodified large-scale spectral energy densities. Explicit diffusion of moisture scalars seems to have only little impact on the bulk heat budget and on convective precipitation. This could hypothetically be related to a dominating role of dry convection for the initiation of deep precipitating convection, but a numerical explanation will be provided in the next section.

## 5. The origin of grid-scale energy

The emerging hypothesis is that energy at small scales may grow because of the presence of convective instabilities, and lead to a mesoscale signal primarily because of the presence of complex underlying topography. Still, it is unclear what mechanisms cause the initial buildup of grid-scale energy. Its existence could either be due to turbulent kinetic energy contained in resolved convective updrafts, or due to spurious effects of numerical origin.

### a. Formulation of moisture advection

To distinguish between physically meaningful and numerically generated energy at the grid scale we perform further experiments with moisture advection schemes that exhibit different small-scale behavior. This method has also been used by Bryan (2005) to study spurious cloud patterns in idealized simulations of squall lines. We compare our previous simulations using the positive-definite (PD) second-order Bott scheme against the PD and monotonic van Leer scheme (van Leer 1977), and against a semi-Lagrangian scheme (SL). The SL advection scheme is described in Staniforth and Côté (1991) and has been tested within the COSMO model by Förstner et al. (2006). The SL scheme produces more pronounced grid-scale oscillations than Bott's formulation, but reveals similar dissipative characteristics (Förstner et al. 2006). As also indicated by Förstner et al. (2006), the van Leer scheme provides monotonicity at the expense of stronger numerical diffusion.

Figure 13a shows a comparison of the mean diurnal cycles of precipitation produced by the three advection schemes. All three simulations have been carried out with and without explicit diffusion applied to moisture scalars (simulations Q1 and NODIFF, respectively). Obviously, the impact of explicit diffusion of moisture

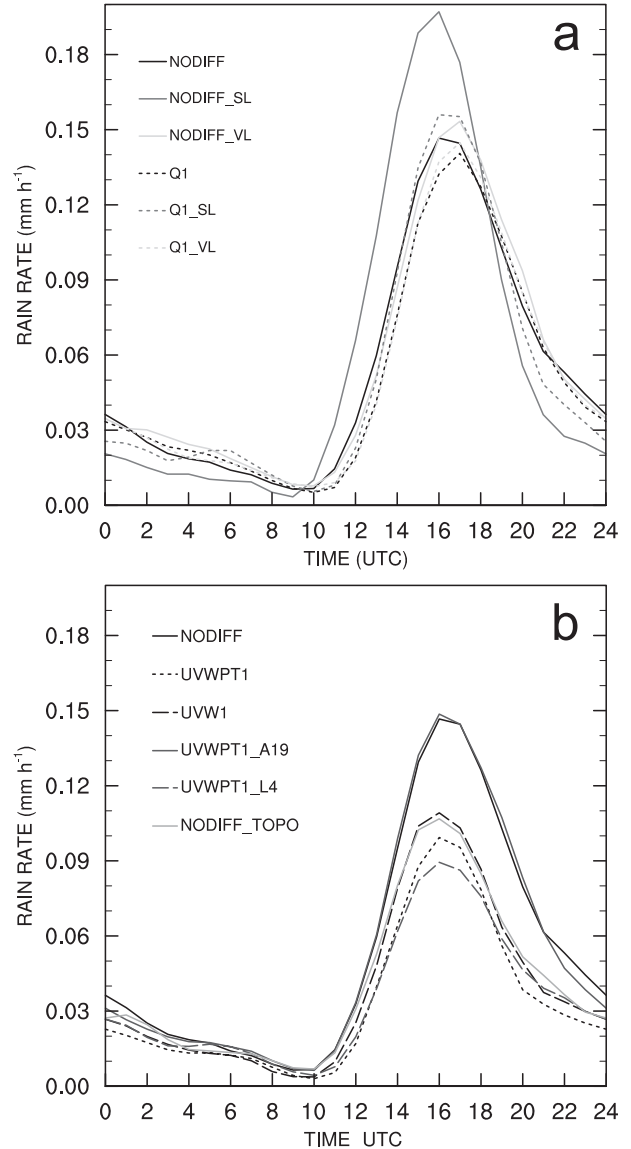


FIG. 13. As in Fig. 5, but (a) for simulations using three different moisture advection schemes. Runs have been conducted with and without explicit diffusion of moisture scalars (simulations Q1 and NODIFF, respectively); (b) for simulations with explicit numerical diffusion restricted to selected model levels (A19 = above level 19, L4 = lowermost 4 levels) and a simulation with enhanced topographic filtering but without diffusion (simulation NODIFF\_TOPO).

scalars for the van Leer type of advection (NODIFF\_VL and Q1\_VL) is as small as for the Bott-type advection. In contrast, the SL scheme without explicit diffusion (NODIFF\_SL) results in an increase of the mean daytime precipitation peak by 34% and an earlier onset indicates faster initiation of moist convection. Applying explicit diffusion to moisture scalars (Q1\_SL) drastically reduces convective precipitation and adjusts also the

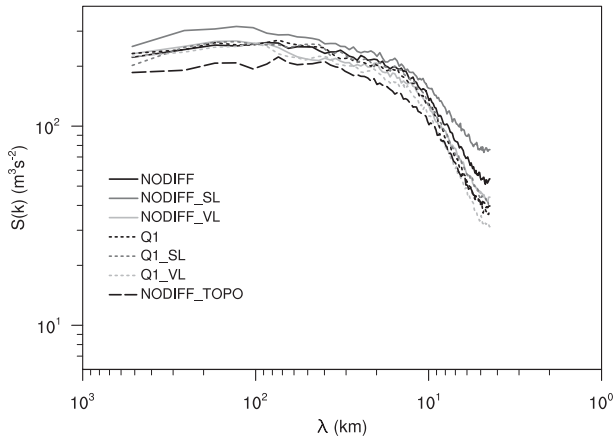


FIG. 14. Average spectra of vertical velocity computed for the Alpine subdomain at 4000 m MSL and 1600 UTC. Different moisture advection schemes have been applied for simulations using (solid) no explicit diffusion and (short dashed) diffusion of moisture scalars. A strongly filtered topography has been used in NODIFF\_TOPO.

timing of precipitation to the diurnal cycles resulting from the other two schemes.

The spectral analysis of vertical velocity (see Fig. 14) shows that the mesoscale dynamics differ between NODIFF\_SL and the other simulations, with the former containing more variance also at the Alpine scale. Note that the application of the PD flux limiter is sufficient to control the amplification of computational noise, whereas the additional effect due to monotonicity appears to be small.<sup>2</sup> Compared to NODIFF the maximum net heating within the upper troposphere is increased by 27% in NODIFF\_SL (not shown).

These findings are in agreement with the simulations conducted by Bryan (2005) and strengthen the importance of adequate (i.e., positive definite or better non-oscillating) numerical formulations for cloud-permitting applications.

#### b. Explicit diffusion on selected levels

So far explicit diffusion has been applied equally on all model levels. To clarify which levels correspond to a source of grid-scale energy, we conduct further simulations with explicit diffusion applied only on a selected range of vertical levels. Figure 13b shows the mean diurnal cycle of precipitation of two additional simulations, for which strong diffusion of the variables is applied only on levels clearly above the PBL (UVWPT1\_A19) and on the lowest four levels (UVWPT1\_L4), respectively. Table 2 adds information about the quantitative modifications of

precipitation with respect to NODIFF. UVWPT1\_A19 has hardly any impact on the mean Alpine precipitation rates (Fig. 13b), while UVWPT1\_L4 decreases the convective precipitation significantly.

The resulting bulk temperature tendencies of simulation UVWPT1\_L4 (not shown) are comparable to the findings from simulation UVWPT1 (Fig. 11). We conclude that the grid-scale perturbations stem from model levels close to the surface, where surface heating results in slope flows and dry convective instabilities. We also suspect, besides physically meaningful small-scale instabilities, numerically introduced disturbances from the computation of temperature and momentum advection and of the horizontal pressure gradient on steep model surfaces (e.g., Janjić 1989) to be significant.

#### c. Topography

To quantify the role of another source for grid-scale energy, namely the underlying small-scale topography, also a simulation NODIFF\_TOPO with enhanced topographic filtering is conducted. To this end we shift the 50% cutoff-wavenumber  $k_c$  from  $4.7\Delta x$  to  $6.8\Delta x$ , by increasing  $\epsilon$  from 10 to 1000 [Eq. (1)]. NODIFF\_TOPO results in a similar reduction of precipitation as UVW1 (see Fig. 13b), since compared to NODIFF the availability of small-scale fluctuations is reduced (see Fig. 14). This result is plausible as small-scale topography, although some filtering is applied, induces grid-scale perturbations of mostly physical origin. Again, suppressing the initial buildup of grid-scale energy affects the whole spectrum (see Fig. 14).

Overall, the simulations presented in this section confirm that the buildup of grid-scale energy is to some degree of numerical origin, but also related to dynamics over mountainous terrain. The buildup is significantly stronger for oscillating (and thus noisy) schemes, operates primarily in the boundary layer, and depends significantly upon the underlying topography. The experiments also demonstrate that the optimum choice of horizontal diffusion will strongly depend upon the numerical formulation of the model under consideration.

## 6. Linear theory and explicit diffusion

In this section linear theory of convective growth is used to enhance our understanding of the diverse impact of explicit diffusion on the growth of near-surface grid-scale energy. Linear stability theory (LST) of thermal convection has originally been used to determine the external factors responsible for an unstable growth of convective overturning between differentially heated rigid plates (i.e., Rayleigh–Bénard convection; e.g., Drazin 2002). More recently, Fuhrer and Schär (2005)

<sup>2</sup> Note that positive-definite advection of a  $q'_C$  perturbation within an unsaturated ( $\overline{q}_C = 0$ ) environment is even monotonic.

determined characteristic growth times of cellular convection embedded in flow over a mountain ridge and showed that horizontal second-order diffusion shifts the fastest-growing modes to larger scales.

Here, we closely follow their method, but add to the given set of linearized Boussinesq-approximated equations the right-hand-side diffusion operators, which are used in the numerical model described in section 2. The modified set of momentum, temperature, and continuity equation, written as

$$\frac{\partial u}{\partial t} + \bar{U} \frac{\partial u}{\partial x} = -\frac{1}{\bar{\rho}} \frac{\partial p}{\partial x} + K_M \frac{\partial^2 u}{\partial z^2} - \nu_h \Delta^2 u, \quad (5)$$

$$\frac{\partial v}{\partial t} + \bar{U} \frac{\partial v}{\partial x} = -\frac{1}{\bar{\rho}} \frac{\partial p}{\partial y} + K_M \frac{\partial^2 v}{\partial z^2} - \nu_h \Delta^2 v, \quad (6)$$

$$\frac{\partial w}{\partial t} + \bar{U} \frac{\partial w}{\partial x} = -\frac{1}{\bar{\rho}} \frac{\partial p}{\partial z} + K_M \frac{\partial^2 w}{\partial z^2} - \nu_v \Delta^2 w - B, \quad (7)$$

$$\frac{\partial B}{\partial t} + \bar{U} \frac{\partial B}{\partial x} = -N^2 w + K_H \frac{\partial^2 B}{\partial z^2} - \nu_b \Delta^2 B, \quad (8)$$

$$\nabla \cdot \mathbf{v} = 0, \quad (9)$$

includes the explicit fourth-order horizontal diffusion (third term on rhs) and for consistency also the second-order vertical turbulent mixing (second term on rhs) operators. Here,  $\Delta = \partial^2/\partial x^2 + \partial^2/\partial y^2$  is the horizontal Laplacian. The parameters  $K_M$  and  $K_H$  are the eddy-diffusion coefficients for momentum and heat, respectively. The hyperviscosities  $\nu_h$ ,  $\nu_v$ , and  $\nu_b$  determine the magnitude of horizontal explicit diffusion of horizontal velocities  $u$  and  $v$ , vertical velocity  $w$ , and buoyancy  $B = gT'/\bar{T}$ , respectively, and are chosen in agreement with the numerical simulations as  $\nu = \nu_1$  (see also section 2). In analogy to the numerical sensitivity experiments described above, here the modifications of characteristic growth times  $\tau$  (i.e.,  $e$ -folding time) due to explicit horizontal diffusion of specific variables is investigated. Wave solutions of the form

$$\{u, v, w, p, B\} = \{\hat{u}, \hat{v}, \hat{w}, \hat{p}, \hat{B}\} e^{i(kx+ly+mz-\omega t)}, \quad (10)$$

are substituted into the set of Eqs. (5)–(9). Hereby,  $k$ ,  $l$ , and  $m$  are the horizontal and vertical wavenumbers, respectively. We derive a general dispersion relation for the complex frequency  $\omega$ , which is not shown here because of its complexity. The relation can be simplified under the assumption of equal hyperviscosities  $\nu_h = \nu_v = \nu_b \equiv \nu$  and equal eddy-diffusion coefficients  $K_M = K_H \equiv K$  to

$$\omega = k\bar{U} - i[\nu(k^4 + l^4) + Km^2] \pm i\sqrt{-N^2} \left( \frac{k_h^2}{k_h^2 + m^2} \right)^{1/2}, \quad (11)$$

with  $k_h = (k^2 + l^2)^{1/2}$  and the Brunt–Väisälä frequency  $N$ . Without diffusion ( $\nu = 0$ ,  $K = 0$ ) the dispersion relation reduces to Eq. (10) in Fuhrer and Schär (2005). The real part related to the Doppler-shifted frequency  $k\bar{U}$  is subtracted from  $\omega$ , such that the characteristic growth time, given by  $\tau = i/(\omega - k\bar{U})$ , is independent of  $\bar{U}$ . As an example, under the simplifications used to derive Eq. (11), the characteristic growth time becomes

$$\tau = \left[ -\nu(k^4 + l^4) - Km^2 \pm \sqrt{-N^2} \left( \frac{k_h^2}{k_h^2 + m^2} \right)^{1/2} \right]^{-1}. \quad (12)$$

Note that in Eqs. (11) and (12) only the first solution is physically meaningful with larger instabilities (more negative  $N^2$ ) causing larger frequencies  $\omega$  and smaller growth times  $\tau$ . Obviously, both horizontal and vertical diffusion in Eq. (12) reduce the convective growth and counteract the growth due to thermal instability.

Figure 15 shows characteristic growth times obtained from the full dispersion relation using different assumptions for the hyperviscosities  $\nu_h$ ,  $\nu_v$ , and  $\nu_b$ . For this study we have chosen  $N^2 = -2 \times 10^{-5} \text{ s}^{-2}$  and a typical value of  $10 \text{ m}^2 \text{ s}^{-1}$  [see Stull (1988), p. 206] for the turbulent momentum diffusion  $K_M$ . The Prandtl number is assumed to be unity ( $K_H = K_M$ ). The growth time is given for amplifying grid-scale perturbations with  $\lambda_h = 2\Delta x$  and  $\lambda_z = 2 \text{ km}$  on top of Figs. 15a–f. As has been shown by Fuhrer and Schär (2005), a strongly anisotropic perturbation (thin and deep) will grow most rapidly without diffusion (see Fig. 15a). The modulation of growth rates due to this anisotropy can be understood by substituting the horizontal velocities from Eqs. (5)–(6) into the continuity Eq. (9). This yields the relation between vertical acceleration and the vertical pressure gradient, written for the inviscid case and in Fourier-space as

$$-i\omega \hat{w} = \frac{i m \hat{p}}{\bar{\rho}} \left( \frac{1}{m k_h^{-1}} \right)^2. \quad (13)$$

It can be seen that thin and deep disturbances ( $m k_h^{-1} < 1$ ) are related to stronger vertical acceleration than broad and shallow ones ( $m k_h^{-1} > 1$ ).

Figures 15b–f demonstrate that due to vertical turbulent diffusion only sufficiently deep perturbations can grow, while shallow perturbations decay in time. Explicit horizontal diffusion shifts the fastest-growing modes to

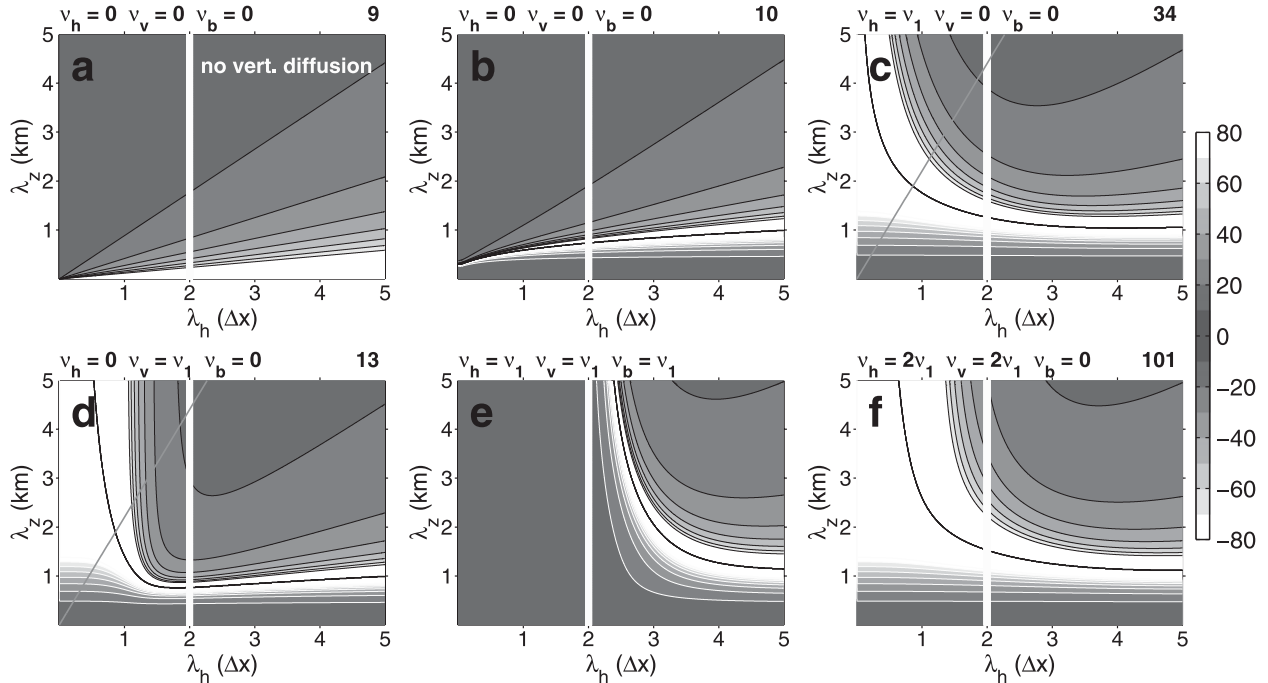


FIG. 15. (a)–(f) Characteristic growth times (minutes) of linear normal modes in dependence of horizontal and vertical wavelength of the unstable air parcel. The instability within the parcel is assumed to be  $N^2 = -2 \times 10^{-5} \text{ s}^{-2}$  and the horizontal diffusion coefficients are given on top (a)–(f) together with the growth time of a parcel with horizontal and vertical wavelengths  $\lambda_h = 2\Delta_h$  and  $\lambda_v = 2 \text{ km}$ , respectively. White contour lines indicate negative (stable) values. Vertical diffusion is neglected only in (a). The smallest resolved horizontal waves are given by the bold white lines. The gray lines in (c) and (d) correspond to  $\lambda_h = \lambda_v$ .

larger horizontal wavelengths (Figs. 15c–f). Growth times are increased especially for the grid-scale perturbations (e.g.,  $\lambda_h = 2\Delta_x$ ). Explicit horizontal diffusion of horizontal momentum (see Fig. 15c) results in significant increase of the grid-scale growth times. Applying numerical diffusion additionally to vertical velocity (not shown) causes only a minor increase of the growth times compared to the results shown in Fig. 15c. Also, Fig. 15d demonstrates that the fastest-growing modes are still of the size of grid-scale perturbations for diffusion only applied to vertical velocity. Interestingly, the resulting growth times due to buoyancy diffusion alone are identical to the results from diffusion applied to the three wind components (which is similar to Fig. 15c and therefore both are not shown). Rapid decay of grid-scale convective instabilities occurs in the case of both momentum and buoyancy perturbations (Fig. 15e). The decaying modes do not arise because of an additive increase of the diffusion rates, since the doubling of  $\nu_h$  and  $\nu_v$  (Fig. 15f) has far less impact on growth times than the nonlinear effect due to additional buoyancy diffusion.

These findings are in line with the numerical experiments, which indicated that particularly explicit diffusion of horizontal momentum components and/or buoyancy contributes to a shift of the fastest-growing modes to

larger horizontal wavelengths, while explicit diffusion of vertical velocity still supports the fastest-growing perturbations of grid-scale size.

To further investigate this, the dispersion relation for horizontal diffusion applied to either horizontal velocities, vertical velocity, or buoyancy is written in a more general form (for  $K_M = K_H = 0$ ) as

$$\begin{aligned} \omega_{h,v,b} = k\bar{U} - i\frac{1}{2}\nu_{h,v,b}A_{h,v,b}(k^4 + l^4)C \\ + \sqrt{-\frac{1}{4}\nu_{h,v,b}^2(k^4 + l^4)^2A_{h,v,b}^2C^2 + CN^2}, \end{aligned} \quad (14)$$

with  $C = (1 + m^2k_h^{-2})^{-1}$  and the coefficients  $A_h = m^2k_h^{-2}$ ,  $A_v = 1$ ,  $A_b = C^{-1}$ . Factor  $C$  describes a faster growth of small anisotropies  $mk_h^{-1} < 1$ , which affects the buoyancy-driven growth even in the inviscid case [see Eq.(12)]. The additional anisotropies  $A$  are related to the specific horizontal diffusion terms. Only for isotropic scales (see gray lines in Figs. 15c,d), which will not be realized on highly anisotropic (sheetlike) grids of convection-permitting models, the growth rates resulting from diffusion of vertical velocity and horizontal velocity, respectively, become identical. Note that diffusion of buoyancy affects the vertical velocity directly through the buoyancy

acceleration term in Eq. (7), but also indirectly because of the coupling with the continuity equation (thus  $A_b = A_v + A_h$ ). Therefore, the reduction of convective growth is larger for diffusion of buoyancy than for diffusion applied to either vertical or horizontal velocities, except for the limits  $mk_h^{-1} \rightarrow 0$  ( $\omega_b = \omega_v$ ) and  $mk_h^{-1} \rightarrow \infty$  ( $\omega_b = \omega_h$ ).

The agreement between numerical experiments and LST, which is capable of explaining only the initial, linear phase of convective growth, indicates that the sensitivity to explicit diffusion is due to the slowdown of the linear amplification of grid-scale perturbations. Note that on the other hand the complexity introduced by orography is not considered by the theoretical approach and also subsidence in the dry surrounding, which decreases the effective buoyancy within the rising moist plume (Kirshbaum and Smith 2009), is not accounted for. The fact that we assume an infinitely periodically repeating perturbation in space might further explain the agreement with the analyzed bulk properties of several convective plumes.

## 7. Discussion

In agreement with Bryan (2005) our results emphasize an important caveat of convection-permitting simulations: the overlap of numerically contaminated scales with the scales of single convective plumes. Thus, numerical noise may act as an additional trigger for initial small-scale convective growth. As shown in the current study, this may influence the mesoscale flow through upscaling. The amount of numerical noise will depend, among other factors, on the diffusivity and dispersivity of the advection scheme. As demonstrated in section 5a and shown by Bryan (2005) adequate discretizations of advection (e.g., positive definite or nonoscillating) allow for a reduction of the numerical noise contained at the grid scale. The NODIFF simulation, which uses a minimal setup of numerical diffusion and applies a noise-reducing positive-definite advection for moisture scalars, reveals considerably less energy at both small scales and well-resolved scales than the same simulation but applying a dispersive semi-Lagrangian scheme for the advection of moisture scalars (see Fig. 14).

Since the development of deep convection is influenced by instabilities in subsaturated layers near the surface (see section 5b), a similar reduction of both grid-scale and mesoscale energy can be expected for an improved formulation of temperature and momentum transport. Thus, together with aliasing errors, NODIFF still contains numerical noise at the grid scale and therefore requires sufficient explicit diffusion. This is supported by a comparison to radar observations, which demonstrated that NODIFF triggers convection at too many locations and produces too many grid-scale updrafts. However, it is certainly

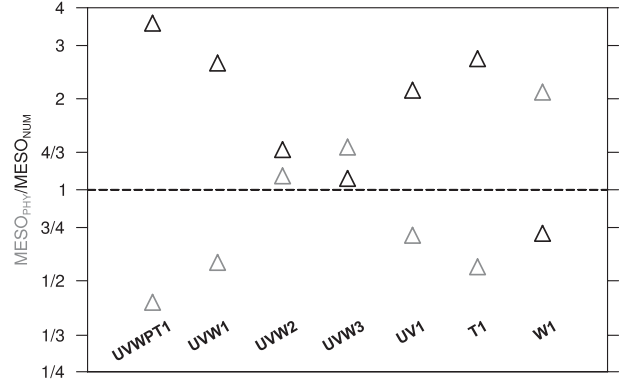


FIG. 16. Ratios of reductions of vertical velocity variance at the mesoscale ( $517 \text{ km} > \lambda > 20 \text{ km}$ ) computed from vertical velocity spectra averaged at 1600 UTC for simulations using different setups of explicit diffusion. MESO<sub>NUM</sub> and MESO<sub>PHY</sub> are plotted using a logarithmic scale and both are defined in the text. It is argued that configurations with  $\text{MESO}_{\text{NUM}} \approx 1$  and  $\text{MESO}_{\text{PHY}} > 1$  yield an optimal model setup, which for the current model is the case for UVW2 and UVW3.

extremely challenging to separate numerically generated from physically meaningful energy at the grid scale, as both numerical inaccuracies and aliasing errors are barely quantifiable. A general recommendation for explicit diffusion in convection-permitting models is thus likely not possible.

Still, for the applied setup of the COSMO model an appropriate choice for explicit numerical diffusion can be made by comparing the reduction of mesoscale energy due to improved small-scale transport against the reduction of mesoscale energy due to explicit diffusion. To account for numerical errors still present in NODIFF (despite improved moisture advection), the damping due to explicit filtering should be similar in magnitude as the expected impact from improved numerics. Too strong explicit filtering will deteriorate the physically meaningful grid-scale dynamics, such as slope and valley flows in complex terrain, whereas insufficient filtering allows an amplification of grid-scale energy. To objectively account for these properties, we use the quantity MESO<sub>NUM</sub> (see Fig. 16). It has been computed from the reductions  $D$  of mesoscale 1600 UTC average variance  $S(k)$  of the vertical velocity (see also Figs. 8 and 14) as

$$\begin{aligned} \text{MESO}_{\text{NUM}} &= \frac{D_{\text{EXPL}}}{D_{\text{PD}}} \\ &= \frac{\int_{k_l}^{k_s} [S(k)_{\text{NODIFF}} - S(k)] dk}{\int_{k_l}^{k_s} [S(k)_{\text{NODIFF\_SL}} - S(k)_{\text{NODIFF}}] dk}, \end{aligned} \quad (15)$$

with wavenumbers  $k_l = 2\pi(517 \text{ km})^{-1}$  and  $k_s = 2\pi(20 \text{ km})^{-1}$ . It relates the integrated mesoscale reduction  $D_{\text{EXPL}}$  of a simulation's variance  $S(k)$  due to explicit filtering to the expected reduction  $D_{\text{PD}}$  due to improved small-scale numerical advection. Values below 1 indicate insufficient diffusion of numerical noise, while values larger than 1 pinpoint an unnecessarily strong grid-scale filtering.

We also demonstrated that the mesoscale impact of strong momentum diffusion is similar to the influence stemming from the underlying small-scale topography (see Fig. 14). An upper-limit to explicit diffusion applied in simulations over complex terrain can thus be seen in the mesoscale response to increased terrain-filtering, which substantially affects physically meaningful grid-scale flows. To this end we define  $\text{MESO}_{\text{PHY}}$  as

$$\begin{aligned} \text{MESO}_{\text{PHY}} &= \frac{D_{\text{TOPO}}}{D_{\text{EXPL}}} \\ &= \frac{\int_{k_l}^{k_s} [S(k)_{\text{NODIFF}} - S(k)_{\text{NODIFF_TOPO}}] dk}{\int_{k_l}^{k_s} [S(k)_{\text{NODIFF}} - S(k)] dk}, \end{aligned} \quad (16)$$

which is the ratio of the reduction  $D_{\text{TOPO}}$  of mesoscale energy due to increased topographic filtering to the reduction due to explicit filtering  $D_{\text{EXPL}}$ . For  $\text{MESO}_{\text{PHY}} < 1$  the mesoscale energy removed by explicit filtering is even larger than the contribution provided by an upscaling of energy related to small-scale topography. This is certainly not aspire as computational costs to resolve topography should be compensated by more detailed realizations of topographic circulations.

Figure 16 shows that numerical noise in W1 is expected to grow at the grid-scale ( $\text{MESO}_{\text{NUM}} < 1$ ). Unnecessarily strong damping of the convective growth is observed for UVWPT1, UVW1, UV1, and T1 ( $\text{MESO}_{\text{NUM}} > 2$ ). This is reflected also in a too-heavy impact compared to the filtering of physical-meaningful grid-scale flows ( $\text{MESO}_{\text{PHY}} < 1$ ). Apparently, an appropriate mesoscale impact of explicit diffusion is given in UVW2 and UVW3. Particularly UVW3 (weak diffusion of momentum) has significantly less influence on the mesoscale than additional topographic filtering, while still damping as sufficiently as would be expected from improved numerical discretizations. Thus, for the used setup of COSMO we recommend to apply moderate explicit diffusion only to the velocity components. Thereby, the effect on the physical solution is kept small (in contrast to explicit diffusion applied to the velocities *and* to the buoyancy), while preventing the accumulation of kinetic energy at the grid

scales. However, note that this estimate is based on the assumption, that a reduction of existing numerical noise in NODIFF (due to improved momentum or temperature advection) yields a mesoscale energy reduction similar to the reductions gained from improved moisture advection ( $D_{\text{PD}}$ ). Still, this suggestion is supported by Thuburn (2008), who highlights the importance of the grid-scale removal of downscaled kinetic energy, and by the fact that explicit horizontal diffusion of buoyancy and moisture, which is commonly computed along terrain-following model levels, results in artificial vertical transport of heat and moisture over complex terrain (Zängl 2002).

## 8. Summary and conclusions

Numerical simulations with the nonhydrostatic COSMO model have been conducted using a grid spacing of 2.2 km. The impact of fourth-order explicit diffusion has been investigated for a period of summertime diurnal convection over a large Alpine domain. As expected, the numerical experiments reveal reductions of grid-scale energy due to explicit diffusion, which directly result in modifications of the grid-scale dynamics.

Moreover, our results show that small-scale numerical diffusion in a convection-permitting model is decisive not only for the representation of grid-scale cloud structures, but also for the mesoscale flow behavior:

- A reduction of mesoscale dynamical activity over the mountain range (“alpine pumping”) manifests an upscale influence of explicit diffusion. The widespread triggering of orographic convection over the mountain range is found to establish mountain-scale vertical motions.
- Explicit diffusion is capable of reducing the bulk Alpine advective heating within the PBL, since significantly less heat transport occurs from the surface upward around midday. Additionally, less precipitating deep convective plumes are triggered and thereby the bulk latent heating can be decreased by up to 30% in the upper troposphere.
- The average surface precipitation is reduced by up to 37% in simulations using relatively large diffusion coefficients.

The upscaling underlines the influence of small-scale convective growth on mesoscale dynamics. Thus, in this study, additional simulations and arguments derived from linear stability theory (LST) have been employed to clarify the sensitivity of the small-scale convective growth to explicit diffusion:

- The convective growth is controlled particularly by explicit diffusion of horizontal momentum and buoyancy

- close to the surface, while diffusion applied to vertical velocity has little impact; this is in line with an increase of characteristic growth times of thermal instabilities, which have been determined using LST.
- LST suggests that only for isotropic convective scales, which are typically not simulated in an under-resolved convective PBL, the damping of convective growth due to explicit diffusion of horizontal and vertical velocity, respectively, becomes identical.

Our findings further demonstrated that a separation of numerical noise from physically meaningful energy at the grid scale is notoriously difficult in convection-permitting simulations over terrain. In our COSMO simulations weak explicit diffusion applied to velocities resulted in a removal of grid-scale energy such that the mesoscale impact was just as large as expected from improved (i.e., noise reducing) formulations of advection. Stronger diffusion (or additional diffusion of buoyancy) decreased the convective growth and precipitation significantly and revealed a nonphysically large mesoscale damping even larger than the mesoscale uptake of energy provided by an upscaling of energy due to the presence of topographic flows. However, since the required grid-scale filtering will be linked to the formulation of the numerics and to the application (e.g., type of flow) a general recommendation cannot be provided.

An apparent strategy to the encountered sensitivity would be to avoid simulations at kilometer scales, which is, however, unfavorable as convection-permitting models reveal several advantages over convection-parameterizing models (see the introduction). In addition, large-eddy simulations (LES) are not yet affordable for many applications, and they require much finer grid spacings to allow numerical simulations of the energy-containing scales without contamination by numerical discretizations and aliasing errors (Ghosal 1996). Additional work is thus needed to assess numerical convergence of simulations at convection-permitting scales and to define the optimal treatment of turbulence and diffusion at the grid scale.

**Acknowledgments.** This work has been funded by and established in the framework of the Center for Climate System Modeling (C2SM) at ETH Zurich. We thank Cathy Hohenegger and MeteoSwiss (especially Oliver Fuhrer and Tanja Weusthoff) for constructive discussions. The Swiss National Supercomputing Centre (CSCS) is acknowledged for providing access to its high-performance compute clusters; access to the COSMO model was kindly provided by the COSMO consortium. We would also like to acknowledge constructive comments by two anonymous referees.

## REFERENCES

- Blackadar, A. K., 1962: The vertical distribution of wind and turbulent exchange in a neutral atmosphere. *J. Geophys. Res.*, **67**, 3095–3102.
- Bott, A., 1989: A positive definite advection scheme obtained by nonlinear renormalization of the advective fluxes. *Mon. Wea. Rev.*, **117**, 1006–1015.
- Bryan, G. H., 2005: Spurious convective organizations in simulated squall lines owing to moist absolutely unstable layers. *Mon. Wea. Rev.*, **133**, 1978–1997.
- , J. C. Wyngaard, and J. Fritsch, 2003: Resolution requirements for simulations of deep moist convection. *Mon. Wea. Rev.*, **131**, 2394–2416.
- Colle, B. A., and C. F. Mass, 2000: The 5–9 February 1996 flooding event over the Pacific Northwest: Sensitivity studies and evaluation of the MM5 precipitation forecasts. *Mon. Wea. Rev.*, **128**, 593–617.
- Craig, G. C., and A. Dörnbrack, 2008: Entrainment in cumulus clouds: What resolution is cloud-resolving? *J. Atmos. Sci.*, **65**, 3978–3988.
- Denis, B., J. Côté, and R. Laprise, 2002: Spectral decomposition of two-dimensional atmospheric fields on limited-area domains using the Discrete Cosine Transform (DCT). *Mon. Wea. Rev.*, **130**, 1812–1829.
- Doms, G., and U. Schättler, 2002: A description of the Non-hydrostatic Regional Model LM. Part I: Dynamics and numerics. Tech. Rep. LM\_F90 2.18, COSMO, 140 pp. [Available online at <http://www.cosmo-model.org>.]
- Drazin, P. G., 2002: *Introduction to Hydrodynamic Instability*. Cambridge University Press, 258 pp.
- Durran, D. R., 1999: *Numerical Methods for Wave Equations in Geophysical Fluid Dynamics*. Springer-Verlag, 465 pp.
- Förstner, J., and G. Doms, 2004: Runge–Kutta time integration and high-order spatial discretization of advection—A new dynamical core for the LMK. *Model Development and Application, COSMO Newsletter*, No. 4, COSMO, 168–176. [Available online at <http://www.cosmo-model.org/content/model/documentation/newsLetters/newsLetter04/chp9-6.pdf>.]
- , M. Baldauf, and A. Seifert, 2006: Courant number independent advection of the moisture quantities for the LMK. *Working Group on Numerical Aspects, COSMO Newsletter*, No. 6, COSMO, 51–64. [Available online at [http://www.cosmo-model.org/content/model/documentation/newsLetters/newsLetter06/cnl6\\_foerstner.pdf](http://www.cosmo-model.org/content/model/documentation/newsLetters/newsLetter06/cnl6_foerstner.pdf).]
- Fuhrer, O., and C. Schär, 2005: Embedded cellular convection in moist flow past topography. *J. Atmos. Sci.*, **62**, 2810–2828.
- Gage, K. S., and G. D. Nastrom, 1985: On the spectrum of atmospheric velocity fluctuations seen by MST/ST radar and their interpretation. *Radio Sci.*, **20**, 1339–1347.
- Ghosal, S., 1996: An analysis of numerical errors in large-eddy simulations of turbulence. *J. Comput. Phys.*, **125**, 187–206.
- Grell, G. A., L. Schade, R. Knoche, A. Pfeiffer, and J. Egger, 2000: Nonhydrostatic climate simulations of precipitation over complex terrain. *J. Geophys. Res.*, **105**, 595–608.
- Heise, E., M. Lange, B. Ritter, and R. Schrödin, 2003: Improvement and validation of the multi-layer soil model. *Model Development and Application, COSMO Newsletter*, No. 3, COSMO, 198–203. [Available online at <http://www.cosmo-model.org/content/model/documentation/newsLetters/newsLetter03/cnl3-chp9-12.pdf>.]

- Hohenegger, C., P. Brockhaus, and C. Schär, 2008: Towards climate simulations at cloud-resolving scales. *Meteor. Z.*, **17**, 383–394.
- , —, C. S. Bretherton, and C. Schär, 2009: The soil moisture–precipitation feedback in simulations with explicit and parameterized convection. *J. Climate*, **22**, 5003–5020.
- Janjić, Z. I., 1989: On the pressure gradient force error in  $\sigma$ -coordinate spectral models. *Mon. Wea. Rev.*, **117**, 2285–2292.
- Kirshbaum, D. J., and R. B. Smith, 2009: Orographic precipitation in the tropics: Large-eddy simulations and theory. *J. Atmos. Sci.*, **66**, 2559–2578.
- Knievel, J. C., G. H. Bryan, and J. P. Hacker, 2007: Explicit numerical diffusion in the WRF model. *Mon. Wea. Rev.*, **135**, 3808–3824.
- Lean, H., and P. A. Clark, 2003: The effects of changing resolution on mesoscale modelling of line convection and slantwise circulations in FASTEX IOP16. *Quart. J. Roy. Meteor. Soc.*, **129**, 2255–2278.
- , —, M. Dixon, N. M. Roberts, A. Fitch, R. Forbes, and C. Halliwell, 2008: Characteristics of high-resolution versions of the Met Office Unified Model for forecasting convection over the United Kingdom. *Mon. Wea. Rev.*, **136**, 3408–3424.
- Mellor, G. L., and T. Yamada, 1982: Development of a turbulence closure model for geophysical fluid problems. *Rev. Geophys. Space Phys.*, **20**, 851–875.
- MeteoSchweiz, cited 2006: Juli 2006: Klimatologisch ein extremer Monat. [Available online at [http://www.meteoschweiz.admin.ch/web/de/wetter/wetterereignisse/juli\\_2006\\_erste\\_bilanz.html](http://www.meteoschweiz.admin.ch/web/de/wetter/wetterereignisse/juli_2006_erste_bilanz.html).]
- Petch, J. C., 2006: Sensitivity study of developing convection in a cloud-resolving model. *Quart. J. Roy. Meteor. Soc.*, **132**, 345–358.
- Piotrowski, Z. P., P. K. Smolarkiewicz, S. P. Malinowski, and A. A. Wyszogrodski, 2009: On the numerical realizability of thermal convection. *J. Comput. Phys.*, **228**, 6268–6290.
- Raschendorfer, M., 2001: The new turbulence parameterization of LM. *COSMO Newsletter*, No. 1, COSMO, 90–98. [Available online at <http://www.cosmo-model.org>.]
- Raymond, W. H., 1988: High-order low-pass implicit tangent filters for use in finite area calculations. *Mon. Wea. Rev.*, **116**, 2132–2141.
- Reinhardt, T., and A. Seifert, 2006: A three-category ice-scheme for LMK. *Working Group in Physical Aspects, COSMO Newsletter*, No. 6, 115–120. [Available online at [http://www.cosmo-model.org/content/model/documentation/newsLetters/newsLetter06/cnl6\\_reinhardt.pdf](http://www.cosmo-model.org/content/model/documentation/newsLetters/newsLetter06/cnl6_reinhardt.pdf).]
- Ritter, B., and J. F. Geleyn, 1992: A comprehensive radiation scheme for numerical weather prediction models with potential applications in climate simulations. *Mon. Wea. Rev.*, **120**, 303–325.
- Schär, C., D. Leuenberger, O. Fuhrer, D. Lüthi, and G. Girard, 2002: A new terrain-following vertical coordinate for atmospheric prediction models. *Mon. Wea. Rev.*, **130**, 2459–2480.
- Schmidli, J., and R. Rotunno, 2010: Mechanisms of along-valley winds and heat exchange over mountainous terrain. *J. Atmos. Sci.*, **67**, 3033–3047.
- Skamarock, W. C., 2004: Evaluating mesoscale NWP models using kinetic energy spectra. *Mon. Wea. Rev.*, **132**, 3019–3032.
- , and M. L. Weisman, 2009: The impact of positive-definite moisture transport on NWP precipitation forecasts. *Mon. Wea. Rev.*, **137**, 488–494.
- Staniforth, A., and J. Côté, 1991: Semi-Lagrangian integration schemes for atmospheric models—A review. *Mon. Wea. Rev.*, **119**, 2206–2223.
- Steppeler, J., G. Doms, U. Schättler, H. W. Bitzer, A. Gassmann, U. Damrath, and G. Gregoric, 2003: Meso-gamma scale forecasts using the nonhydrostatic model LM. *Meteor. Atmos. Phys.*, **82**, 75–96.
- Stull, R. B., 1988: *An Introduction to Boundary Layer Meteorology*. Kluwer Academic Publishers, 666 pp.
- Takemi, T., and R. Rotunno, 2003: The effects of subgrid model mixing and numerical filtering in simulations of mesoscale cloud systems. *Mon. Wea. Rev.*, **131**, 2085–2101; Corrigendum, **133**, 339–341.
- Thuburn, J., 2008: Some conservation issues for the dynamical cores of NWP and climate models. *J. Comput. Phys.*, **227**, 3715–3730.
- van Leer, B., 1977: Towards the ultimate conservative difference scheme. IV. A new approach to numerical convection. *J. Comput. Phys.*, **23**, 276–299.
- VanZandt, T. E., 1982: A universal spectrum of buoyancy waves in the atmosphere. *Geophys. Res. Lett.*, **9**, 575–578.
- Weisman, M. L., W. C. Skamarock, and J. B. Klemp, 1997: The resolution dependence of explicitly modeled convective systems. *Mon. Wea. Rev.*, **125**, 527–548.
- Weissmann, M., F. Braun, L. Ganter, G. J. Mayr, S. Rahm, and O. Reitebuch, 2005: The Alpine mountain–plain circulation: Airborne Doppler lidar measurements and numerical simulations. *Mon. Wea. Rev.*, **133**, 3095–3109.
- Wicker, L. J., and W. C. Skamarock, 2002: Time-splitting methods for elastic models using forward time schemes. *Mon. Wea. Rev.*, **130**, 2088–2097.
- Wüest, M., M. Litschi, A. Altenhoff, C. Frei, M. Hagen, and C. Schär, 2010: A gridded hourly precipitation dataset for Switzerland using rain-gauge analysis and radar-based disaggregation. *Int. J. Climatol.*, **30**, 1764–1775.
- Zängl, G., 2002: An improved method for computing horizontal diffusion in a sigma-coordinate model and its application to simulations over mountainous topography. *Mon. Wea. Rev.*, **130**, 1423–1432.
- , 2004: The sensitivity of simulated orographic precipitation to model components other than cloud microphysics. *Quart. J. Roy. Meteor. Soc.*, **130**, 1857–1875.
- , 2007: Small-scale variability of orographic precipitation in the Alps: Case studies and semi-idealized numerical simulations. *Quart. J. Roy. Meteor. Soc.*, **133**, 1701–1716.